

Supplemental Materials for

Three-dimensional mineral dendrites reveal a nonclassical crystallization pathway

Zhaoliang Hou¹, Dawid Woś², Cornelius Tschegg³, Anna Rogowitz^{4,1}, A. Hugh N. Rice¹, Lutz Nasdala⁵, Florian Füsseis⁶, Piotr Szymczak^{2*}, Bernhard Grasemann^{1*}

This file includes:

Supplemental material 1. Methods; Figs. S1A and B

Supplemental material Fig. S2. Sample description

Supplemental material Fig. S3. Dendrite geochemistry data

Supplemental material Fig. S4. Numerical Vs. Natural dendrites

References for supplemental materials

Other supplementary materials for this manuscript include the following:

Movies S1

Movies S2

SUPPLEMENTAL MATERIAL 1. METHODS

32 dendrite samples were collected; seven were scanned using X-ray microtomography, imaging 236 individual mineral dendrites; polished thin-sections of nine specimens were made perpendicular to the fracture surface after being embedded in epoxy resin.

1.1 Structural observations

Three-dimensional microtomographic data were acquired from mm-sized samples at the School of Geosciences, University of Edinburgh. For X-ray imaging, a transmission X-ray source was used with 120 keV peak energy and 2.8 W power loading (W target on diamond). For each dataset, 2000 projections were collected over a 360° sample rotation in evenly spaced intervals, at a 2s exposure for each 1 MP projection. From these projections, virtual image stacks representing the samples were reconstructed with the Octopus v 8.9 software (Dierick et al., 2004), using a filtered back projection algorithm, yielding a stack of 8-bit images (1024×1024 pixels) with a voxel size of 9µm. The image stacks were then processed and visualized using ImageJ (Schneider et al., 2012). The image stacks were denoised using a mean filter (Radius: 1). Dendrite structures were segmented using Weka Trainable Segmentation (Arganda-Carreras et al., 2017). Dendrite forest and internal structures were visualized using 3D script (Schmid et al., 2019). Dendrite volume and 3D fractal dimensions were calculated using "Voxel Counter" and "fractal count" plugins respectively.

Polished thin-sections of dendrites were imaged with a Keyence VHX-5000 digital microscope (DM), using HDR-mode reflected light. The Line-intersection technique was used on binary DM mosaic; successive horizontal straight-lines across each sample at every 100 pixels (~270µm) from the forest bottom to the top, parallel to the fracture surface, were used to calculate total and average dendrite thickness as a function of distance from the fracture surface.

Electron-dispersive X-ray spectroscopy (EDS) and backscattered electron (BSE) imaging were performed on a FEI INSPECT-S50 scanning electron microscope (SEM) with beam conditions of 15 kV and 15 nA. Secondary electron imaging was performed on a FEI QUANTA 3D FEG instrument with beam conditions of 10KV and 4 nA. Binary pore maps were segmented from BSE images using Weka Trainable Segmentation. Porosity variations were calculated by contouring area fractions of the segmented pores (> 90% confidence) from each unit area (307×307 pixels).

1.2 Geochemistry

Electron probe micro-analysis (EPMA) line-scan analyses of polished sections were made using a Cameca SXFive FE electron probe micro-analyzer (15 keV acceleration voltage; 20 nA beam current). Detecting beam size was 10 μm in diameter, with an analytical spacing of 10 μm . Detection limit of manganese oxides is 0.05 wt.%.

Raman spectra were obtained using a dispersive Horiba LabRAM HR Evolution system equipped with Olympus BX-series optical microscope and Peltier-cooled, Si-based charge-coupled device detector. The sample material was found to be sensitive to heavy light absorption (i.e. thermal degradation within the focal-spot area, seen from "burned" spots) under 532 nm and 633 nm excitation, and, in addition, spectra obtained with 633 nm excitation were obscured by a fairly intense background. Raman spectra were therefore excited with the 473 nm emission of a diode laser (3 mW at the sample). A 100 \times objective (numerical aperture 0.90) was used to focus the light onto the sample surface and to collect the Raman-scattered light. The system was operated in the confocal mode, resulting in a lateral resolution of better than 1 μm (cf. [Kim et al., 2020](#)). The light to be analyzed was dispersed with a 1800 grooves per mm diffraction grating. More experimental details are described in [Zeug et al. \(2018\)](#).

XRD analyses were done on a Bruker XRD, scanning at 0.015° step intervals and 0.15 s per interval.

1.3 Numerical modelling

Our numerical model is an extension of the classical reaction-diffusion model of 2-D mineral dendrite growth (Chopard, 1991). In detail, we assume that the system was infiltrated by a Mn-rich fluid moving through a fracture network. This fluid invades the rock matrix, pushing an alkaline and oxygenated pore fluid away from the fracture surface. Due to mixing at the interface between the two fluids, a solution oversaturated with manganese oxide appears.

In detail, we are solving the coupled convection-diffusion-reaction equations for the concentrations of oxygen molecules, c_{O_2} , and manganese ions, c_{Mn} . These two species can react with each other, forming nanoparticles of concentration c_p . The equations describing the dynamics of this process are

$$\begin{aligned}\frac{\partial c_{O_2}}{\partial t} &= D_{O_2} \nabla^2 c_{O_2} - k c_{O_2} c_{Mn} \\ \frac{\partial c_{Mn}}{\partial t} &= D_{Mn} \nabla^2 c_{Mn} - k c_{O_2} c_{Mn}\end{aligned}$$

for oxygen molecules and manganese ions and

$$\frac{\partial c_p}{\partial t} = D_p \nabla^2 c_p + k c_{O_2} c_{Mn} - K$$

for the nanoparticles. Similar models have been proposed for the description of Liesegang patterns (Chopard et al, 1994). In the above, D_{O_2} , D_{Mn} and D_p are the diffusion coefficients of oxygen molecules, manganese ions and manganese oxide nanoparticles, respectively. We have assumed that the kinetics of manganese oxide is linear in both concentrations and irreversible with the kinetic reaction rate k . Finally, K is the reaction term taking into account aggregation

of the nanoparticles on the dendrite; the volume fraction of the dendrite, φ_d correspondingly increases as

$$\frac{\partial \varphi_d}{\partial t} = K v_p$$

The reaction term is nonzero only on the dendrite and along its perimeter, and its magnitude depends on the local surface energy of the dendrite, as described in more detail below.

These equations are solved numerically in either square (in 2D) or cubic (in 3D) domains of length L , representing the area covered by the pulse of manganese-rich fluid. The initial manganese ion concentration within this region was assumed to be uniform, $c_{Mn}(\mathbf{r}, t=0) = c_{Mn}^0$ and the oxygen concentration was assumed to be zero. On the top boundary of the system, $z=L$, we impose the constant oxygen concentration condition, $c_{O_2}(z=L, t) = c_{O_2}^0$, representing the contact with oxygenated fluid above. The bottom boundary, $z=0$, is assumed to be impermeable to both Mn and O₂; along other boundaries we impose periodic boundary conditions. The equations are solved using the solute transport lattice-Boltzmann method (Surkop & Thorne, 2006), discretizing the computational domain into the mesh of 250x250 (2D) or 250x250x250 (3D) points. The topology of the mesh in 2D corresponds to two-dimensional nine-speed model (so called D2Q9 - a square lattice with links to both the nearest and diagonal neighbors and with the rest particles), in 3D the corresponding scheme was D3Q27 with the links to 26 nearest and diagonal neighbors in the cubic lattice).

The aggregation of the particles on the dendrite has been implemented in the following way. First, we identify the set of lattice points, $A(t)$, belonging to the aggregate in a given moment of time as well as the perimeter of this set, $\partial A(t)$, i.e. the lattice points neighboring to A , which are not taken up by the aggregate yet. We allow the nanoparticles to aggregate both on A and ∂A . In the latter case, however, we require that the concentration of nanoparticles

exceeds a threshold c_p^{th} (nucleation condition). When this condition is fulfilled, the nanoparticles can aggregate in a given point of the perimeter and this point becomes an aggregate point from this time on. Additionally, we set the maximum limit on the manganese oxide volume (per unit volume of the rock) that can be precipitated in a given point, $\varphi_d^{max} = 0.1$, which is of the order of total porosity of the clinoptilolite matrix. At the beginning of the simulation, the potential nucleation sites of the dendrite correspond to the bottom boundary ($z=0$), which represents the manganese oxide coated fracture surface, initiating the growth of the mineral dendrite forest.

In the simulations, the ratios of diffusion coefficients of different species were taken to be $D_{Mn} / D_{O_2} = D_p / D_{O_2} = 10$, reflecting the fact that oxygen diffuses faster than the manganese ions and nanoparticles.

In the numerical model, the aggregation itself proceeds in a probabilistic manner, with the local concentration of nanoparticles transferred to a dendrite with a probability that depends on the local radius curvature of the dendrite, R (Vicsek, 1984),

$$p = p_0 + \frac{\Gamma}{R}$$

where $\Gamma = \frac{\sigma v_m}{kT}$ is the capillarity constant, in which σ is the interfacial free energy, v_m is the precipitate molecular volume, k is the Boltzmann constant, and T is the absolute temperature (Mullins and Sekerka, 1963). The local radius of curvature, R , is estimated based on the number of lattice sites occupied by the dendrite in the neighborhood of a given point (Vicsek, 1984; Kadanoff, 1985, Liang, 1985) and $p_0 = \frac{1}{2}$.

There are two important length scales in diffusion-controlled growth processes, the

diffusive length, $\lambda_d = \frac{D_p}{U}$, which is the ratio of the average growth velocity and diffusion

constant and chemical capillary length $\lambda_c = \gamma \Gamma$, where γ is the acid capacity number defined

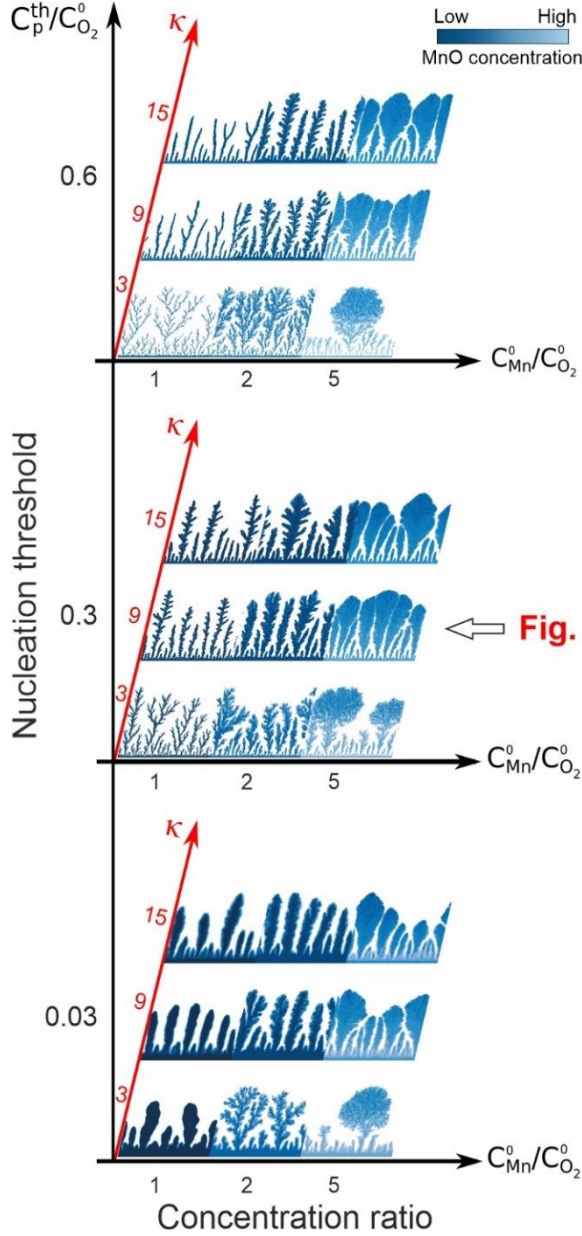


Fig. S1A

Morphologies 2D dendritic patterns as a function of Mn and O₂ concentration ratio and, capillary and diffusive length ratio and the nucleation threshold concentration.

as the number of manganese oxide molecules per unit volume of a dendrite to the number of manganese oxide molecules per unit volume of the precipitating solution (Mullins and Sekerka, 1963, Meakin, 1998, Ladd & Szymczak 2021). The length scales characterizing the morphology of the dendritic forest, λ_m , such as the width of the dendrites or separation between them, are, to the first approximation given by the geometric mean between λ_c and λ_d (Meakin, 1998)

$$\lambda_m = \sqrt{\lambda_c \lambda_d} = \sqrt{\kappa} \lambda_d$$

where $\kappa = \lambda_c / \lambda_d$ is the ratio of the capillary and diffusive length.

The other important parameter in our system is the ratio of the initial Mn concentration to the oxygen concentration imposed on the top boundary of the system, $c_{Mn}^0 / c_{O_2}^0$, and the ratio of nucleation concentration of manganese oxide particles to the oxygen concentration, $c_p^{th} / c_{O_2}^0$ (Fig. S1A). Since we

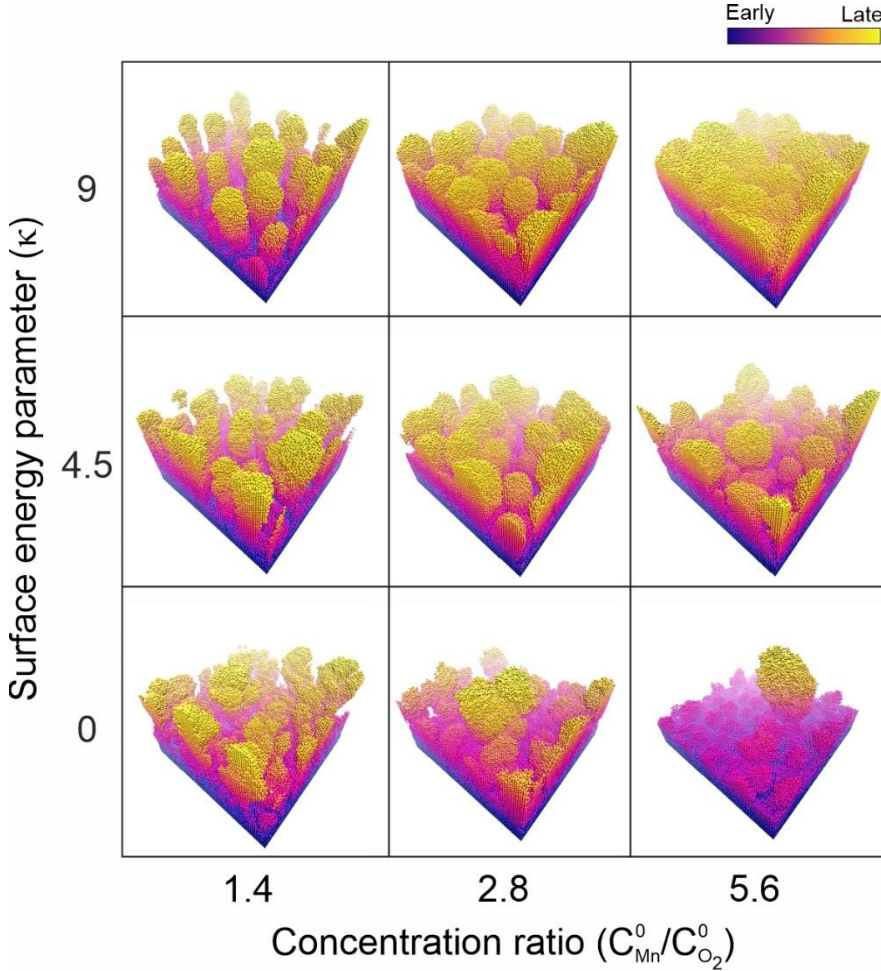
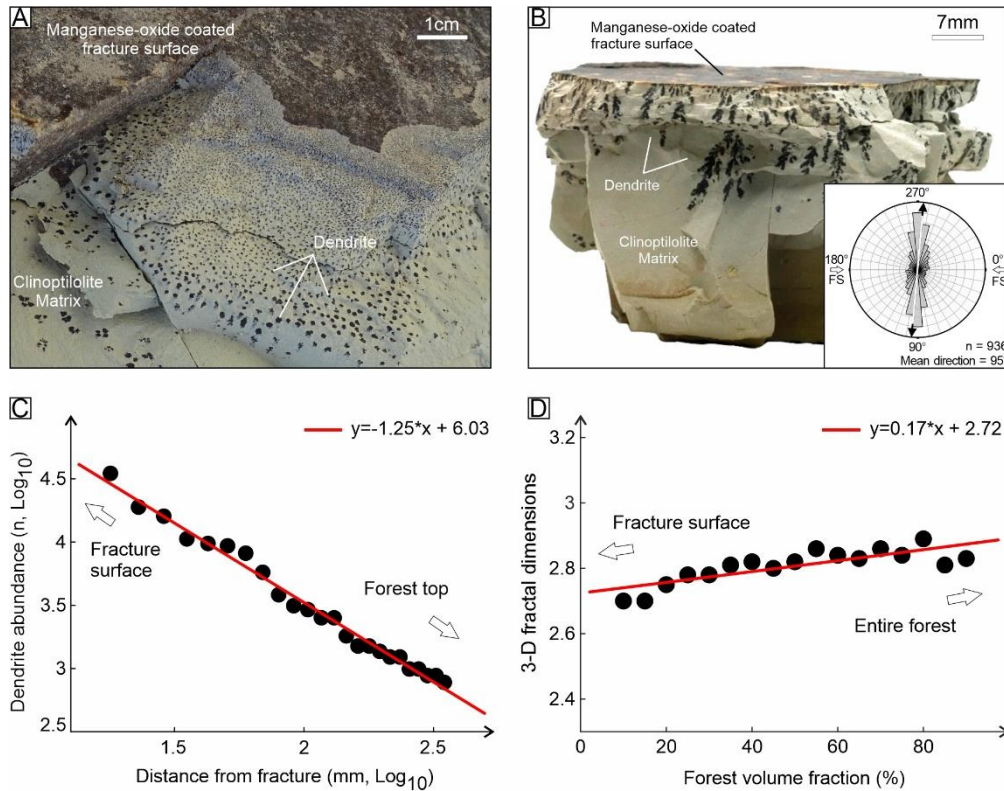


Fig. S1B. Morphologies 3D dendritic patterns. Simulation based on the parameters defined by the 2D simulations.

do not have information what the values of these parameters were in the real system, we analyzed the morphologies of the dendrites for a range of different values of these three ratios ($\kappa, c_{Mn}^0/c_{O_2}^0, c_p^{th}/c_{O_2}^0$) as presented in Supplemental material Fig S4. The comparison of the resulting morphologies with that of the natural dendrite forest in clinoptilolite led us to the conclusion that the latter is

characterized by $\kappa \approx 9, c_{Mn}^0/c_{O_2}^0 \approx 1-2, c_p^{th}/c_{O_2}^0 \approx 0.3$. These estimates will be further modified by the dimensionality of the system. In particular, in 3D the capillary effects (for the same Γ) are two times stronger in 3D than in 2D, hence we expect that κ should be two times smaller in the 3D case, as indeed confirmed in 3D simulations (see Fig. S1B), which show that the morphologies similar to the natural ones are obtained for $\kappa \approx 4.5, c_{Mn}^0/c_{O_2}^0 \approx 1-2, c_p^{th}/c_{O_2}^0 \approx 0.3$

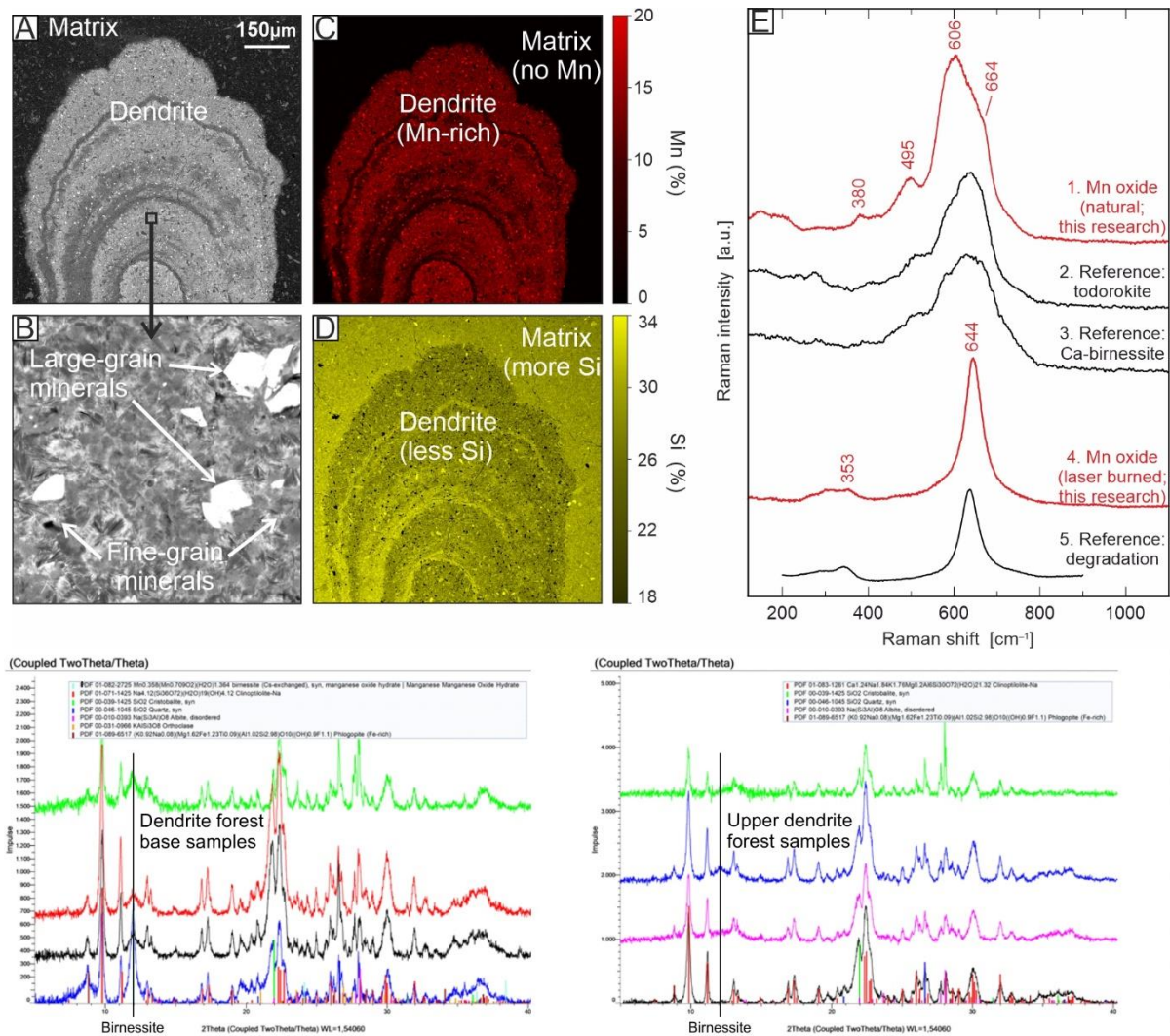
SUPPLEMENTAL MATERIAL FIG. S2. SAMPLE DESCRIPTION



Overview of mineral dendrites in clinoptilolite-tuff. **A**, Irregular surface cutting in-situ clinoptilolite, showing horizontal, oblique and longitudinal sections through the dendrites, revealing their 3-D geometry. **B**, Hand-specimen (also shown in Fig. 1A) showing localization of the mineral dendrites adjacent to a manganese oxide-coated fracture surface, and their branching architecture. Rose-diagram showing dendrite preferred growth orientation relative to the fracture surface (FS). Black arrows with the white line indicate the 095°-275° mean orientation of dendrites, approximately perpendicular to the fracture surface (0°-180°, white arrows). **C**, Power-law scaling of variation in dendrite abundance (n) as forest height increases. Note α is ~ 1.25 . **D**, Variation of forest 3-D fractal dimension as the forest volume increases from the fracture surface. Calculations for both C and D are based on μ CT data.

SUPPLEMENTAL MATERIAL FIG. S3. DENDRITE GEOCHEMISTRY

DATA



Overview of dendrite-forming manganese oxides. **A**, SEM-BSE showing the top part of a mineral dendrites. For details of dendrite internal structure (banding) see the main text and Fig. 2. **B**, Enlargement of **A**. Dendrites comprise fine-grained minerals with euhedral larger minerals. The larger minerals were analysed by Raman spectroscopy. **C-D**, SEM-EDS maps showing dendrite-forming materials; both the fine- and larger-grained minerals are dominated by manganese. **E**, Raman spectra of larger minerals. Top three spectra are low-energy 473 nm excitation; bottom two, high-energy 532 nm excitation. 1 and 4 show the natural Mn oxide from the dendrites. 2 and 3 are reference spectra of poorly ordered todorokite and Ca-birnessite

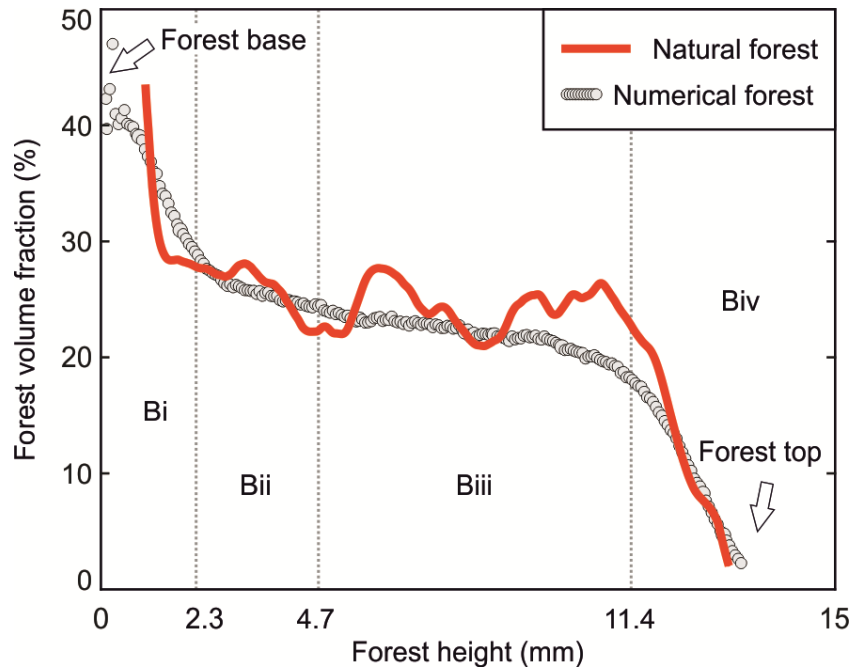
(Abrashv et al., 2019). Reference spectrum of laser-pyrolysed MnO₂ (degradation) from Bernardini et al., 2019.

Reliable assignment to a certain mineral species is virtually impossible, since: (i) spectra depend appreciably on the degree of crystallinity; (ii) spectra of different Mn-oxide minerals show broad similarities, and virtually contradictory spectra are found for the same mineral in the literature; (iii) natural Mn oxides often are heterogeneous mixtures of several phases; and (iv) Mn minerals are sensitive to local heating due to absorption of laser light. In spite of these uncertainties, our spectrum may be assigned to a hydrated Mn-dominated oxide, such as birnessite or todorokite (Julien et al., 2004; Abrashv et al., 2019). see also the spectra of a low-grade Mn ore of Pani et al. (2015). This assignment is apparently supported by the observation that our sample, after thermal degradation due to intense green-laser illumination, yielded a spectrum that is broadly similar to that of green-laser-decomposed pyrolusite (β -MnO₂; see Bernardini et al., 2019).

X-ray diffraction of powdered samples derived by drilling 4 samples, each with a dendrite forest base powder and a upper dendrite forest powder. Low peak intensities indicate that most of the manganese is amorphous. Minor peak intensities reveal birnessite as a typical component in the dendrite forest base and a minor component in one samples from the upper dendrite forest.

Thus both Raman spectroscopy and XRD analyses indicate that there is at least some Mn oxyhydroxides in the dendrites. Whether the amorphous material is an oxyhydroxide is unknown.

SUPPLEMENTAL MATERIAL FIG. S4. NUMERICAL Vs. NATURAL DENDRITES



Comparison of volume fractions in the natural and numerical dendrite forest. Numerical dendrite forest shows a similar volume fraction and volume fraction changes to the natural sample. Forest height is the distance from the fracture surface.

REFERENCE FOR SUPPLEMENTARY MATERIALS

- Abrashev, M.V., Chernev, P., Kubella, P., Mohammadi, M.R., Pasquini, C., Dau, H. and Zaharieva, I., 2019, Origin of the heat-induced improvement of catalytic activity and stability of MnO_x electrocatalysts for water oxidation: *Journal of Materials Chemistry A*, v. 7, p.17022-17036, doi:10.1039/C9TA05108B.
- Arganda-Carreras, I., Kaynig, V., Rueden, C., Eliceiri, K.W., Schindelin, J., Cardona, A. and Sebastian Seung, H., 2017, Trainable Weka Segmentation: a machine learning tool for microscopy pixel classification: *Bioinformatics*, v. 33, p. 2424-2426, doi:10.1093/bioinformatics/btx180.
- Bernardini, S., Bellatreccia, F., Municchia, A.C., Della Ventura, G., Sodo, A., 2019, Raman spectra of natural manganese oxides: *Journal of Raman Spectroscopy*, v. 50, p. 873–888, doi:10.1002/jrs.5583.
- Chopard, B., Herrmann, H.J. and Vicsek, T., 1991, Structure and growth mechanism of mineral dendrites: *Nature*, v. 353, p. 409-412, DOI:10.1038/353409a0.
- Chopard, B., Luthi, P., & Droz, M., 1994, Microscopic approach to the formation of Liesegang patterns: *Journal of statistical physics*, v. 76, p. 661-677, doi:10.1007/BF02188680.
- Dierick, M., Masschaele, B. and Van Hoorebeke, L., 2004, Octopus, a fast and user-friendly tomographic reconstruction package developed in LabView®: *Measurement Science and Technology*, v. 15), p. 1366, doi:10.1088/0957-0233/15/7/020.
- Julien, C.M., Massot, M. and Poinignon, C., 2004, Lattice vibrations of manganese oxides: Part I. Periodic structures. *Spectrochimica Acta Part A: Molecular and Biomolecular Spectroscopy*, v. 60), p. 689-700, 10.1016/S1386-1425(03)00279-8.
- Kadanoff, L. P., 1985, Simulating hydrodynamics: a pedestrian model: *Journal of statistical physics*, v. 39, p. 267-283, doi:10.1007/BF01018663.

- Kim, Y., Lee, E.J., Roy, S., Sharbirin, A.S., Ranz, L.-G., Dieing, T., Kim, J., 2020, Measurement of lateral and axial resolution of confocal Raman microscope using dispersed carbon nanotubes and suspended graphene: *Current Applied Physics*, v. 20, p. 71–77, doi:10.1016/j.cap.2019.10.012.
- Ladd, A. J., & Szymczak, P., 2021, Reactive flows in porous media: Challenges in theoretical and numerical methods: *Annual Review of Chemical and Biomolecular Engineering*, v. 12, p, 543-571, doi: 10.1146/annurev-chembioeng-092920-102703.
- Liang, S., 1986, Random-walk simulations of flow in Hele Shaw cells: *Physical Review A*, v. 33, p. 2663, doi:10.1103/PhysRevA.33.2663.
- Meakin, P., 1998, *Fractals, scaling and growth far from equilibrium, Volume 5*: Cambridge, Cambridge university press, 674p.
- Mullins, W. W., and Sekerka, R. F., 1963, Morphological stability of a particle growing by diffusion or heat flow: *Journal of applied physics*, v. 34, p. 323-329, doi:org/10.1063/1.1702607.
- Pani, S., Singh, S.K., Mohapatra, B.K., 2015, Vibrational spectroscopic study for qualitative assessment of Mn-oxide ore: *Resource Geology*, v. 66, p. 12–23, doi:10.1111/rge.12083.
- Schmid, B., Tripal, P., Fraaß, T., Kersten, C., Ruder, B., Grüneboom, A., Huisken, J. and Palmisano, R., 2019, 3Dscript: animating 3D/4D microscopy data using a natural-language-based syntax: *Nature methods*, v. 16, p. 278-280, doi:10.1038/s41592-019-0359-1.
- Schneider, C.A., Rasband, W.S. and Eliceiri, K.W., 2012, NIH Image to ImageJ: 25 years of image analysis: *Nature methods*, v. 9, p. 671-675, doi:10.1038/nmeth.2089.
- Sukop, M.C and Thorne, D.T., 2010, *Lattice Boltzmann Modelling*: Springer Berlin, Heidelberg.

Vicsek, T., 1984, Pattern formation in diffusion-limited aggregation: Physical review letters, v. 53, p. 2281, doi :10.1103/PhysRevLett.53.2281.

Zeug, M., Nasdala, L., Wanthanachaisaeng, B., Balmer, W.A., Corfu, F. and Wildner, M., 2018, Blue zircon from Ratanakiri, Cambodia: Journal of Gemmology, v. 36, p. 112–132, doi:10.15506/JoG.2018.36.2.112.